RESEARCH ARTICLE-CIVIL ENGINEERING

Investigation on the Large-Deformation Instability Characteristics of Solitary Boulder Slopes by Material Point Method

Lianheng Zhao[1,2] · Zijian Zhang[1] · Shuguang Wang[3] · Nan Qiao[1] · Guoshun Lv[1]

Abstract

Granite rocks are subjected to exogenic forces, such as tectonic stress and chemical weathering, which cause them to weather differentially, forming boulders that are common in temperate and humid regions. The presence of a large boulder on a slope can significantly impact slope stability, resulting in the formation of what is known as a solitary boulder slope. This study is dedicated to investigate the large-deformation instability characteristics of such slopes. In pursuit of this objective, our study first validates an adapted material point method through laboratory experiments. Subsequently, utilizing the inverse discrete Fourier transform theory, boulders with varying shapes were synthesized and further transformed into material point method models. Finally, the material point method was employed to analyse the impact of boulder position, shape, and incline on the large deformation characteristics of the slope. The results show that: (1) The closer a boulder is to the plastic zone of the slope, the stronger its reinforcement effect on the slope. (2) As the shape of boulders becomes more complex, the run-out distance of the slope tends to decrease, but the variability in run-out distances increases. (3) The slope plastic zone moves around the boulder, and its distribution undergoes alterations based on the boulder's shape. This study investigates the instability characteristics of large deformation in boulder slopes with varying boulder shapes, which provides a reference for the stability assessment of solitary boulder slopes.

Keywords Solitary boulder slope · Large-deformation instability · Material point method · Inverse discrete fourier transform · Laboratory model test

✉ Nan Qiao
   qiao.nan@csu.edu.cn

   Lianheng Zhao
   zhaolianheng@csu.edu.cn

   Zijian Zhang
   zzj214812271@csu.edu.cn

   Shuguang Wang
   hnwsg1983@163.com

   Guoshun Lv
   lvgsh20@csu.edu.cn

1 School of Civil Engineering, Central South University, Changsha 410075, People's Republic of China

2 Key Laboratory of Heavy-Haul Railway Engineering Structure, Central South University, Ministry of Education, Changsha 410075, People's Republic of China

3 Guizhou Transportation Planning Surveying Design Research Institute Co, Ltd, Guiyang 550014, Guizhou, People's Republic of China

List of symbols

v_I^s	Velocity contributed by object s at node I
v_I^l	Velocity contributed by object l at node I
n_I^s	Outer normal unit vector of the boundary of object s at node I
D_I^{sl}	Actual distance of s and l at node I
d	Cell size
λ	Point-space coefficient
D_n	Fourier descriptor
H	Slope height (mm)
α	Slope angle (°)
L	Length of the slope crest (mm)
ρ	Density (kg/m^3)
E	Elastic modulus (MPa)
ν	Poisson's ratio
c	Cohesion (kPa)
φ	Friction angle (°)
μ	Friction coefficient

Springer

1 Introduction

Granites often exhibit multiple sets of orthogonal joints, which segment the rocks into distinct sections. Influenced by exogenic forces, such as tectonic stress and chemical weathering, these segments may undergo disparate weathering processes, eventually giving rise to spheroidal weathering formations known as boulders [1–3]. Boulders are a common occurrence in warm and humid regions worldwide, including western and southern Europe, southern Africa, southern Asia, America, and Australia [4]. In hilly and mountainous regions, boulders can become embedded on slopes, and the presence of a substantial boulder on a slope can markedly influence the slope's stability, resulting in what is referred to as a solitary boulder slope.

The geological hazards on slopes, such as rockfalls and landslides, can vary depending on the degree of boulder exposure. A boulder with high exposure is more susceptible to rockfalls because of less support. This phenomenon has been thoroughly studied by other researchers (Pérez-Rey et al. [5, 6]; Vann et al. [7], Gentilini et al. [8], and Morales et al. [9]). On the other hand, a boulder with low exposure can significantly influence the development and distribution of the slope-sliding zone [10, 11]. Surprisingly, this scenario has received relatively little attention in research. Li et al. [12] used the FEM, and Liu et al. [13] used the FDM to discuss the stability of a slope with a completely buried boulder. However, these numerical analysis methods often lead to computational failure owing to grid distortion when the slope deformation is significant, making it challenging to discuss large-deformation failure characteristics such as slip area and failure shape [14].

Furthermore, the original joints of granites are not always entirely orthogonal and the weathering effect on the boulder is not uniform. Hence, the shapes of boulders vary, including ellipsoids, slabs, and other irregular shapes [15, 16] (Fig. 1 displays three boulders with different shapes). Previous studies often overlook these differences when establishing boulder models [5, 7–9] or select a few boulders to create digital models using digital image processing technology [6, 12, 13]. This prevailing approach hinders the quantitative exploration of how the boulder's appearance characteristics affect the characteristics of slope instability.

With advancements in computational science, many new technologies have been introduced in geotechnical engineering. Numerous new methods suitable for large deformation analysis have been proposed [17–19]. Among them, the material point method (MPM) [20, 21] can effectively avoid computational failure caused by grid distortion and use traditional constitutive models of soil and rock. MPM has gradually been applied to slope stability analysis [22, 23], soil excavation [24], anchor pull-out [25], and many other geotechnical engineering fields. Mollon et al. [26] created a new method to generate particles with different shapes based on inverse discrete Fourier transform (IDFT) theory. Relevant researches [26–28] have also demonstrated that Fourier descriptors enable accurate and quantitative control of a particle's elongation, convexity, and surface roughness. These recent developments open up exciting possibilities for investigating the instability characteristics in solitary boulder slopes with large-deformations and for constructing quantitative boulder models reflecting distinct appearance characteristics.

Based on the above analysis, this study aimed to investigate the large-deformation instability characteristics of solitary boulder slopes. First, the modified MPM program was validated using laboratory tests. Second, based on the IDFT, boulder models with different elongations, convexities, and surface roughnesses were quantitatively constructed and placed on regular slopes. Third, these solitary boulder slopes were discretised into MPM models by identifying the soil-boulder boundary. Finally, the MPM program was utilised to explore the influence of boulder position, shape, and inclination degree on the slope run-out distance. The large-deformation mechanisms of solitary boulder slopes were revealed. This study contributes to the evaluation of the solitary boulder slope stability.

Fig. 1 Photographs of three boulders with different shapes

(a) Photograph of boulder one [15]

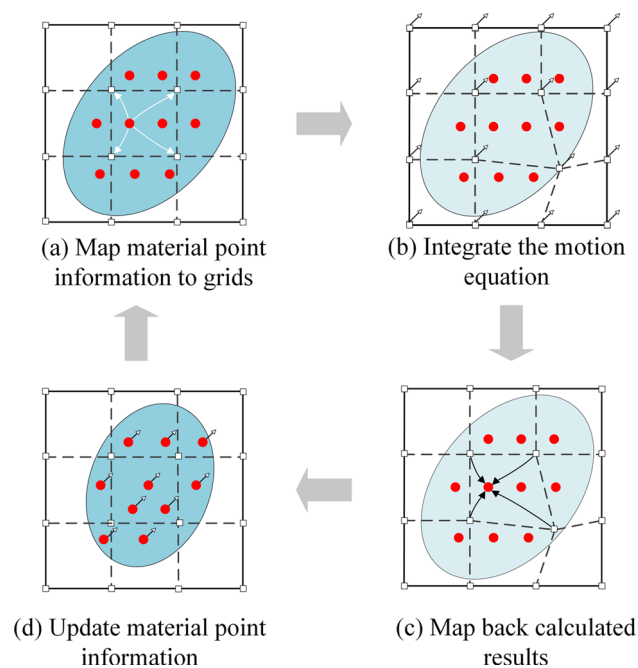(b) Photograph of boulder two

(c) Photograph of boulder three

(a) Map material point
information to grids

(b) Integrate the motion
equation

(d) Update material point
information

(c) Map back calculated
results

Fig. 2 Schematic of the calculation process of MPM

2 Establishment of the MPM Slope Model

2.1 Basic Principle of MPM

2.1.1 Calculation Framework of MPM

MPM combines Lagrange particles and Euler grids to describe the problem domain. In each calculation step, the particles and grids are connected to avoid the generation of nonlinear convection terms. To prevent grid distortion, a new background grid is created at the start of a new step [20, 21].

The MPM calculation framework, as shown in Fig. 2 [29], involves the following steps. (1) The material point information is mapped onto background grids with applied boundary conditions, as shown in Fig. 2a. (2) The motion equation of the grid nodes is integrated by combining the boundary and contact conditions, as shown in Fig. 2b. (3) The calculated results are mapped back to the material points, as shown in Fig. 2c. (4) The position and velocity of the material points are updated, and the deformed meshes are discarded, as shown in Fig. 2d.

2.1.2 Auxiliary Contact Algorithm

In MPM, the motion of objects is determined by the single-value velocity field defined on background grids, and thus, the non-slip contact is automatically satisfied [30]. However, if we want to consider the relative sliding or separation between objects, we need to introduce a contact algorithm. Bardenhagen et al. [31] first introduced a contact algorithm
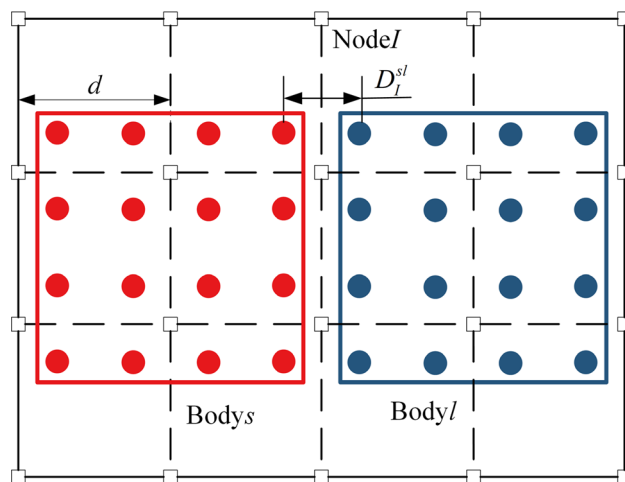

Fig. 3 Schematic of the auxiliary contact algorithm

into MPM, and then many scholars [32, 33] made further improvements to it.

As shown in Fig. 3, if both objects s and l contribute to the momentum of node I, they may come into contact. When the normal velocity of the node satisfies the condition [34]:

$$(v_I^s - v_I^l)n_I^s > 0 \qquad (1)$$

This indicates that the two objects are close to each other and that additional contact force needs to be added [31]. Here, v_I^s is the velocity contributed by object s at node I, v_I^l is the velocity contributed by object l at node I, and n_I^s is the outer normal unit vector of the boundary of object s at node I.

However, Eq. (1) leads to false contact. Although two objects in opposite directions have not actually contacted, when their distance is less than twice the size of the background cell, Eq. (1) is satisfied.

As shown in Fig. 3, to solve this problem, it is necessary to calculate the actual distance D_I^{sl} of two objects to assist the judgment [34]; that is, it also needs to satisfy the condition:

$$D_I^{sl} \leq \lambda d \qquad (2)$$

where the point space coefficient λ is introduced to consider the space area represented by the material point, and d is the cell size.

This study used the MPM calculation program developed by the School of Aerospace, Tsinghua University (https://github.com/xzhang66/MPM3D-F90), which includes some basic contact algorithms [30]. The authors added an auxiliary contact judgment to avoid contact occurring earlier than the actual time.
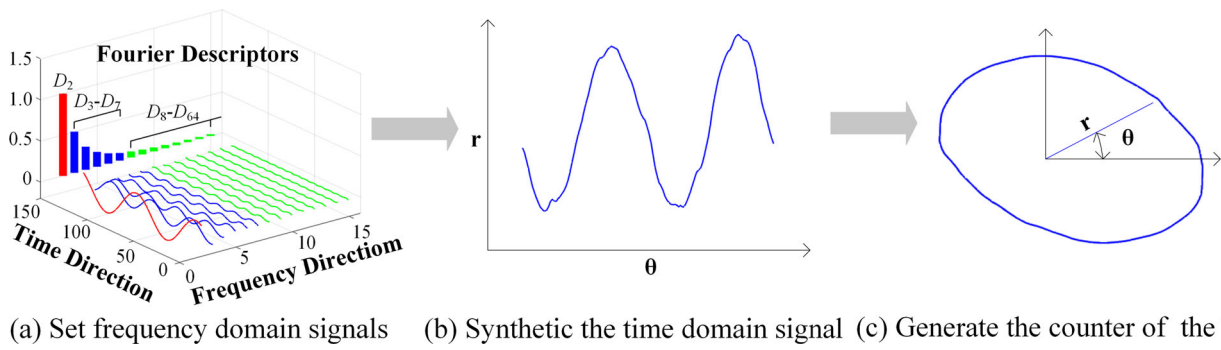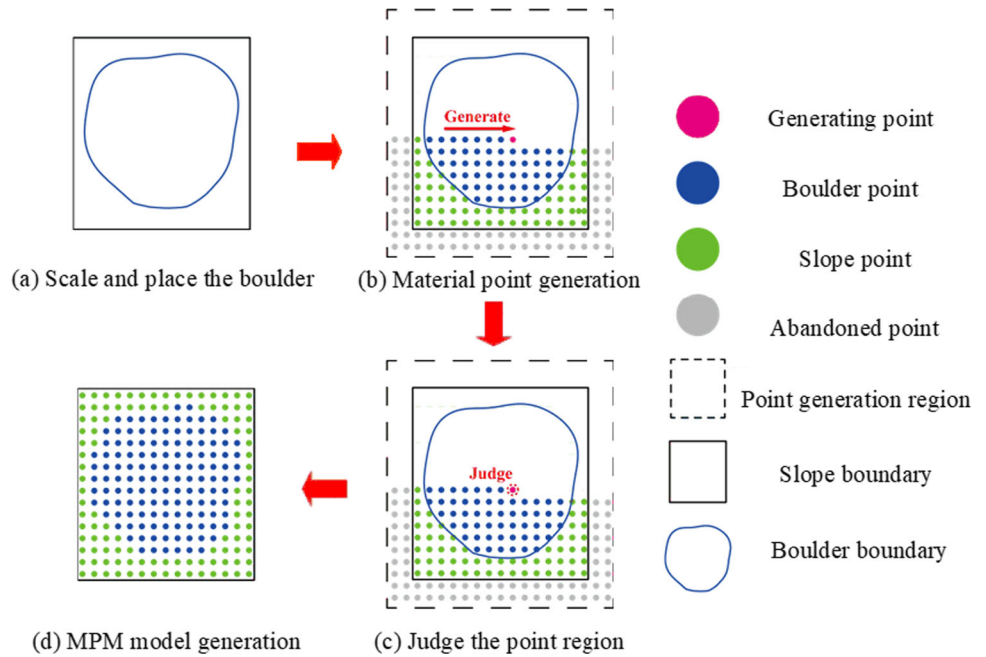
(a) Set frequency domain signals   (b) Synthetic the time domain signal (c) Generate the counter of the boulder

Fig. 4 Schematic of the reconstruction process of the boulder

Fig. 5 Schematic of MPM discretization

(a) Scale and place the boulder   (b) Material point generation

(d) MPM model generation   (c) Judge the point region

Generating point

Boulder point

Slope point

Abandoned point

Point generation region

Slope boundary

Boulder boundary

2.2 Reconstruction of the Boulder Model Based on IDFT

The curve obtained by expanding the contour of the boulder from its centroid can be treated as a time-domain signal in the Fourier domain. According to the Fourier transform, by manipulating discrete frequency-domain signals, it is possible to quantitatively synthesise a time-domain signal and hence construct boulder models with different shapes [26].

In this study, there are 64 discrete frequency-domain signals, and their amplitudes are defined as D_n, which is a Fourier descriptor [26]. Previous studies have shown that controlling D_n can change the shape of the boulder. D_0 and D_1 are fixed values, D_2 controls the elongation of the boulder, and D_3 to D_7 control the convexity of the boulder. D_8 to D_{64} control the surface roughness of the boulder, and their values are obtained from the empirical formulas [26–28]:

$$D_n = 2^{\alpha \cdot \log_2(n/3) + \log_2(D_3)}, \quad 3 < n < 8 \tag{3}$$

$$D_n = 2^{\beta \cdot \log_2(n/8) + \log_2(D_8)}, \quad n > 8 \tag{4}$$

As shown in Fig. 4, discrete frequency-domain signals are generated by controlling the values of D_2, D_3, and D_8. Subsequently, by manipulating these signals, a time-domain signal is constructed to produce a boulder model.

2.3 Discrete of the Solitary Boulder Slope

To use MPM to simulate solitary boulder slopes, it is essential to discretise the model into an MPM model. This study establishes the MPM model by identifying the soil-boulder boundary. The main steps are as follows:

(1) As described in Sect. 3.1, the boulder is reconstructed by Fourier transform, and the boulder model is then scaled and placed on the slope as required, as shown in Fig. 5a.
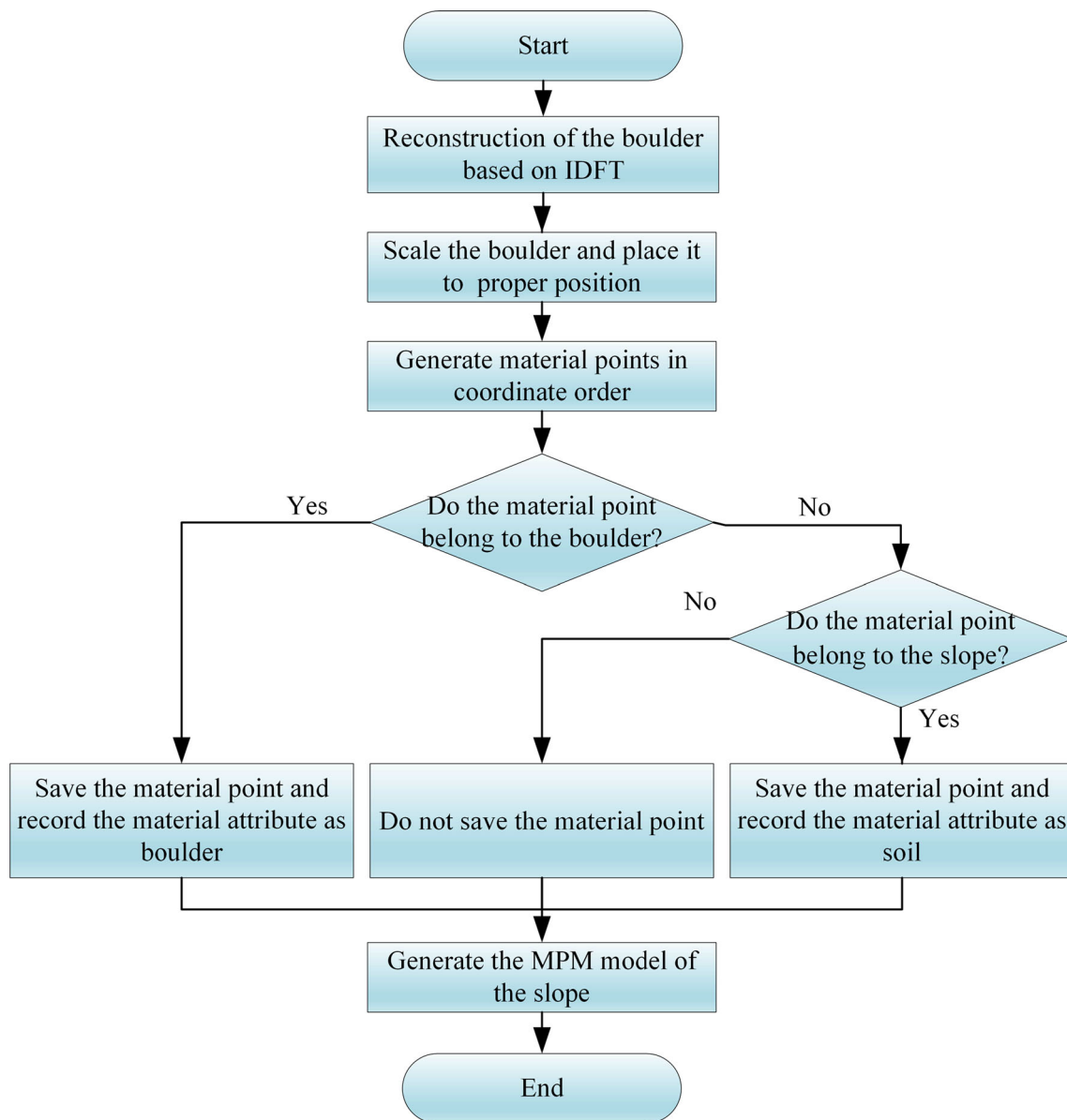
Fig. 6 Flow chart of the generation of the MPM model for the solitary boulder slope

(2) Material points are generated in a designated region according to a predetermined coordinate sequence, as shown in Fig. 5b.

(3) The region to which each material point belonged is identified. If the generated material point belongs to the boulder (blue point in Fig. 5), its attribute is recorded as a boulder. If the generated material point belongs to the soil, it is recorded as the soil (green point in Fig. 5). If the generated material point does not belong to the slope, it is disregarded (grey point in Fig. 5), as shown in Fig. 5c.

(4) The recorded material points are then outputted to generate the MPM model of the slope, as shown in Fig. 5d.

The entire process for generating the MPM model is illustrated in Fig. 6.

3 Laboratory Model Tests

3.1 Test Scheme

To verify the reliability of the MPM program, four laboratory tests on slope failure under gravity were conducted: one homogeneous slope and three heterogeneous slopes. The model box used in the tests is depicted in Fig. 7, and its inner wall size was 1200 mm × 600 mm × 280 mm.
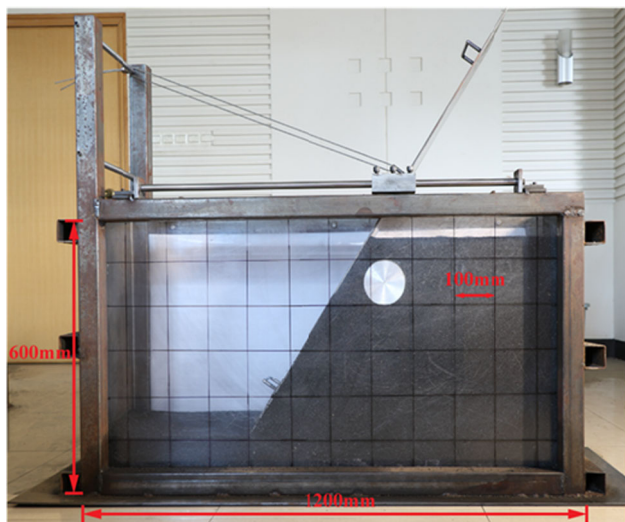
Fig. 7 Model box

Fine gravel with a particle size of 1 mm was used as the soil for the tests. Three aluminium columns with different section shapes but 278 mm in height were used to simulate the boulders. The friction angle was determined through the angle of repose test (Fig. 8a), the friction coefficient was obtained by pulling the aluminium rod using a spring scale (Fig. 8b),

and the density was calculated by measuring the weight and volume ratio of the gravel (Fig. 8c). The remaining parameters, which have a minimal impact on the calculation results, were derived from relevant literature references [35–37]. The specific material parameters and slope geometries are listed in Tables 1 and 2, respectively.

3.2 Test Results

Four indicators were used to compare the results obtained by laboratory tests and the MPM program: run-out distance, influence distance, displacement of the aluminium column, and slope shape after failure. Figure 9 illustrates that the run-out distance is the length difference of the slope bottom before and after slope failure, whereas the influence distance is the length difference of the slope crest before and after slope instability [38].

Table 3 presents the run-out distance, influence distance, displacement of the aluminium column, and relative error between them. Figure 10 shows the laboratory test results and the MPM results, of which I shows the laboratory test results, II shows the MPM results, and III shows the comparison between the tests and the MPM. In addition, there were certain gaps between the aluminium columns and the glass on both sides, and some pebbles may flow into these
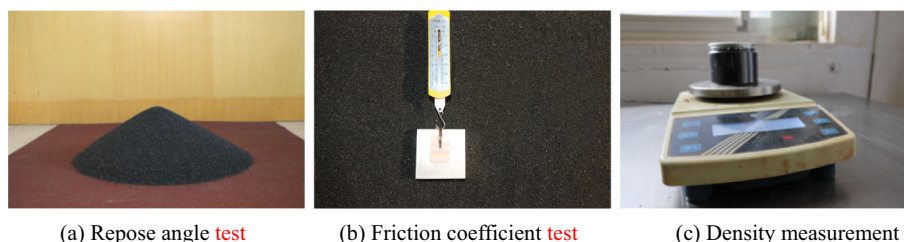
Fig. 8 Measurements of the material parameters

| (a) Repose angle test | (b) Friction coefficient test | (c) Density measurement |

Table 1 Values of material parameters for tests

Material	Density	Poisson's ratio [35]	Elastic modulus [36, 37]	Cohesion	Friction angle	Friction coefficient
	$\rho(\text{kg/m}^3)$	ν	$E(\text{MPa})$	$c(\text{kPa})$	$\varphi(°)$	μ
Gravel	1650	0.20	480	0	36.5	0.35
Aluminium	2700	0.33	70,000	–	–	

Table 2 Sizes of slope models

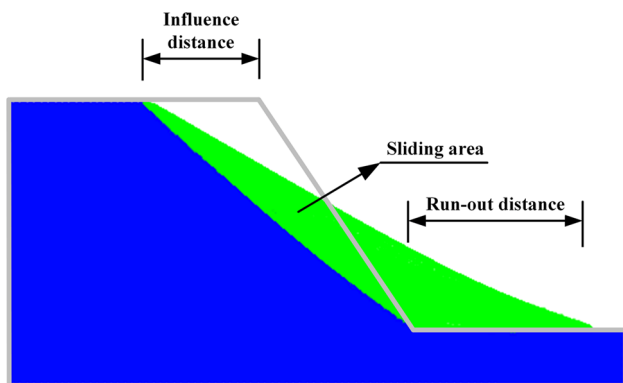| Numb	Slope height	Slope angle	Length of the slope crest	Boulder shape
	$H(\text{mm})$	α (°)	$L(\text{mm})$	
Test 1	495	66.5	400	No boulder
Test 2	495	66.5	400	Circle with the radius of 50 mm
Test 3	450	56.3	400	Square with the side length of 80 mm
Test 4	450	56.3	400	Regular hexagon with the side length of 50 mm

Fig. 9 Schematic of the influence distance and the run-out distance

gaps during movement, and the pebbles in these gaps were processed.

For the homogeneous slope, the results of the laboratory test and MPM solution agreed very well. The relative errors of the run-out distance and influence distance was no more than 15%, which indicated that the adapted program can simulate the large-deformation instability of a homogeneous slope well. For a heterogeneous slope, the aluminium column divided the slope surface into two segments. The first segment was in good agreement, whereas the second had some deviations. Due to dimensional inaccuracies during the fabrication of the model, the acrylic glass does not form a perfectly smooth surface but rather exhibits some curvature. This curvature introduces certain hindrances to the motion of the aluminium column, and the hindering effect increases as the aluminium column move over longer distances. This may be a contributing factor to the larger errors observed in the movement distances of the aluminium column and the deformation of the second portion of the slope.

4 Numerical Analyses

4.1 Model Parameters

Boulders can vary greatly in size and shape owing to differences in their formation environments, with some being

as small as 0.25 m and others larger than 23 m, and taking on various shapes such as spheres, ellipsoids, and irregular slabs [15, 16]. In this study, all boulders were assumed to have an equivalent diameter of 8 m, which is defined as the diameter of an area-equivalent circle. Boulder models are of the stellate category, meaning that there is only one intersection point that radiates from the centroid to the contour of the boulder. The Fourier descriptors D_2, D_3, and D_8 of the boulders used in this study ranged from 0.05 to 0.5, 0.01 to 0.25, and 0.005 to 0.05, respectively. The geometric parameters of the slope model used in this research is depicted in Fig. 11.

The model is assumed to be a plane strain model. The bottom of the model was a fixed boundary, the top was a free boundary, and the rest was a symmetric boundary. Instability was caused solely by dead weight. The Drucker–Prager model was employed to simulate both the soil and boulder, with their material parameters provided in Table 4 [12]. To balance accuracy and efficiency, the grid node spacing was set to 0.20 m, whereas each cell was composed of four material points. The point-space coefficient λ was set to 0.5.

4.2 Influence of the Boulder Position on Run-Out Distance

This section uses five boulder models of different shapes, as illustrated in Fig. 12. Each boulder was buried at the top, middle, or bottom of the slope. The initial position of the boulder centroid was at the slope surface. The boulder located at the top was then vertically displaced downward by 2 m, 4 m, 6 m, 8 m, 10 m, and 12 m. Similarly, the boulder located at the middle is displaced by 2 m, 4 m, 6 m, 8 m, and 10 m, and the boulder at the bottom is displaced by 2 m, 4 m, 6 m, and 8 m, resulting in a total of 18 positions for each boulder and a total of 90 models for the five boulders. Figure 13 shows the various positions of the boulders.

As shown in Fig. 14, different boulder positions have different effects on slope.

When the buried depth was shallow, the run-out distance of the slope with a higher positioned boulder was greater than that with a lower boulder, as shown in Fig. 14a. There are two primary reasons for this phenomenon. First, a boulder at a higher position reinforces less of the soil. Second, a higher

Table 3 Results of the tests and the MPM solutions

Numb	Run-out distance (m)			Influence distance (m)			Displacement of the boulder (m)		
	Test	MPM	Relative error	Test	MPM	Relative error	Test	MPM	Relative error
Test 1	0.460	0.520	13.04%	0.330	0.335	1.52%	–	–	–
Test 2	0.430	0.485	12.79%	0.320	0.371	15.94%	0.278	0.359	29.14%
Test 3	0.270	0.317	17.40%	0.250	0.270	8.00%	0.182	0.224	23.08%
Test 4	0.260	0.328	26.15%	0.280	0.290	3.57%	0.215	0.257	19.53%

(a) Test one

(b) Test two
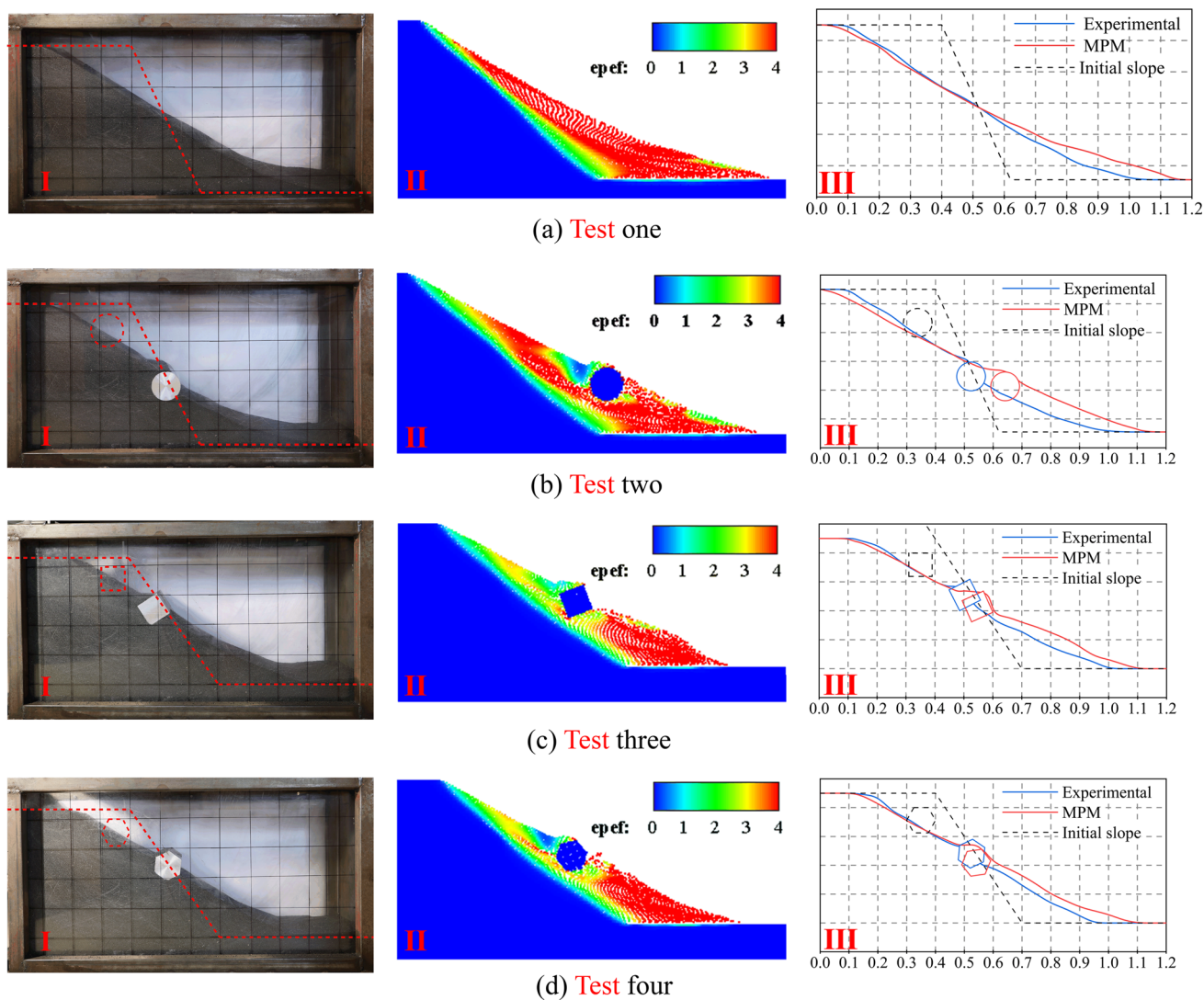

(c) Test three

(d) Test four

Fig. 10 Comparisons of the tests and the MPM solutions

Fig. 11 Schematic of the slope model
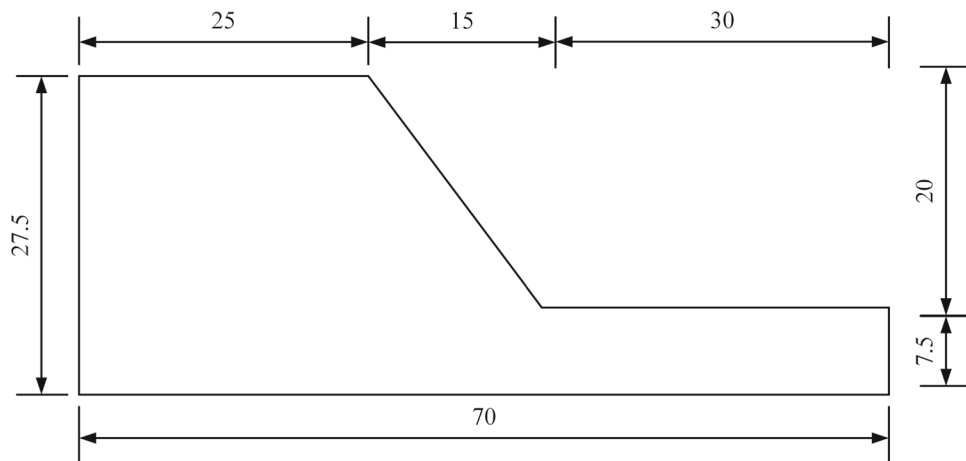
Table 4 Values of material parameters for numerical analysis [12]

Material	Density	Elastic modulus	Poisson's ratio	Cohesion	Friction angle	Friction coefficient
	$\rho(\text{kg/m}^3)$	$E(\text{MPa})$	ν	$c(\text{kPa})$	$\varphi(°)$	μ
Soil	2000	50	0.35	11	18	0.5
Boulder	2500	100,000	0.15	1000	38	
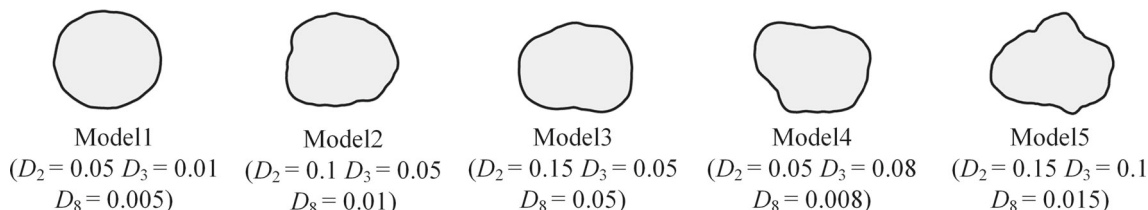
Fig. 12 Five boulder models with different shapes

Model1 ($D_2 = 0.05$ $D_3 = 0.01$ $D_8 = 0.005$)
Model2 ($D_2 = 0.1$ $D_3 = 0.05$ $D_8 = 0.01$)
Model3 ($D_2 = 0.15$ $D_3 = 0.05$ $D_8 = 0.05$)
Model4 ($D_2 = 0.05$ $D_3 = 0.08$ $D_8 = 0.008$)
Model5 ($D_2 = 0.15$ $D_3 = 0.1$ $D_8 = 0.015$)

Fig. 13 Schematic of positions of the boulder
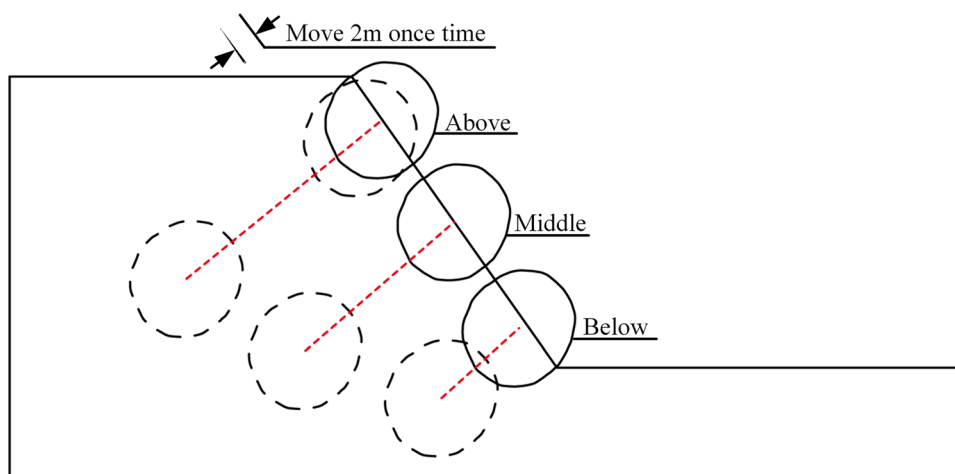
boulder possesses more potential energy, which is released in a more destructive manner when the slope becomes destabilised.

When the buried depth was large, the relationship between the boulder height and run-out distance was less obvious, as shown in Fig. 14a. This is because as the depth increases, the boulder gradually moves away from the sliding zone of the slope, and its reinforcement effect is continuously attenuated. However, the extent of attenuation at different heights is not equal.

For slopes where the boulder was located at the top or middle, the relationship between the run-out distance and burial depth followed a consistent trend, as shown in Fig. 14b and c. With increasing burial depth, the run-out distance initially decreased and then increased. It is worth noting that, for some higher boulders, the run-out distance was larger than that of the homogeneous slope. This phenomenon is attributed to the fact that when the buried depth is shallow, the boulder is located above the sliding zone, and slope instability may be aggravated under the boulder's gravitational force. As the

buried depth increases, the boulder approaches the sliding zone first and then gradually moves away from it, which initially enhances the strengthening effect of the boulder, followed by a subsequent decrease.

For slopes where the boulder was located at the bottom, the run-out distance increased with increasing buried depth, but was always less than that of the homogeneous slope, as shown in Fig. 14d. This is because the boulder at the bottom can reinforce the entire slope. However, with increasing burial depth, the boulder gradually moves away from the sliding zone, leading to a weakening of its reinforcement effect.

4.3 Influence of the Boulder Shape and Inclination Degree on Run-Out Distance

As described in Sect. 3.2, the main indicators used to describe the boulder shape are the elongation, convexity, and surface roughness, which are controlled by Fourier descriptors D_2, D_3, and D_8, respectively. To isolate the impact of each individual factor on the slope, the other descriptors were set to

(a) Mean values at different positions

(b) Boulder at the top

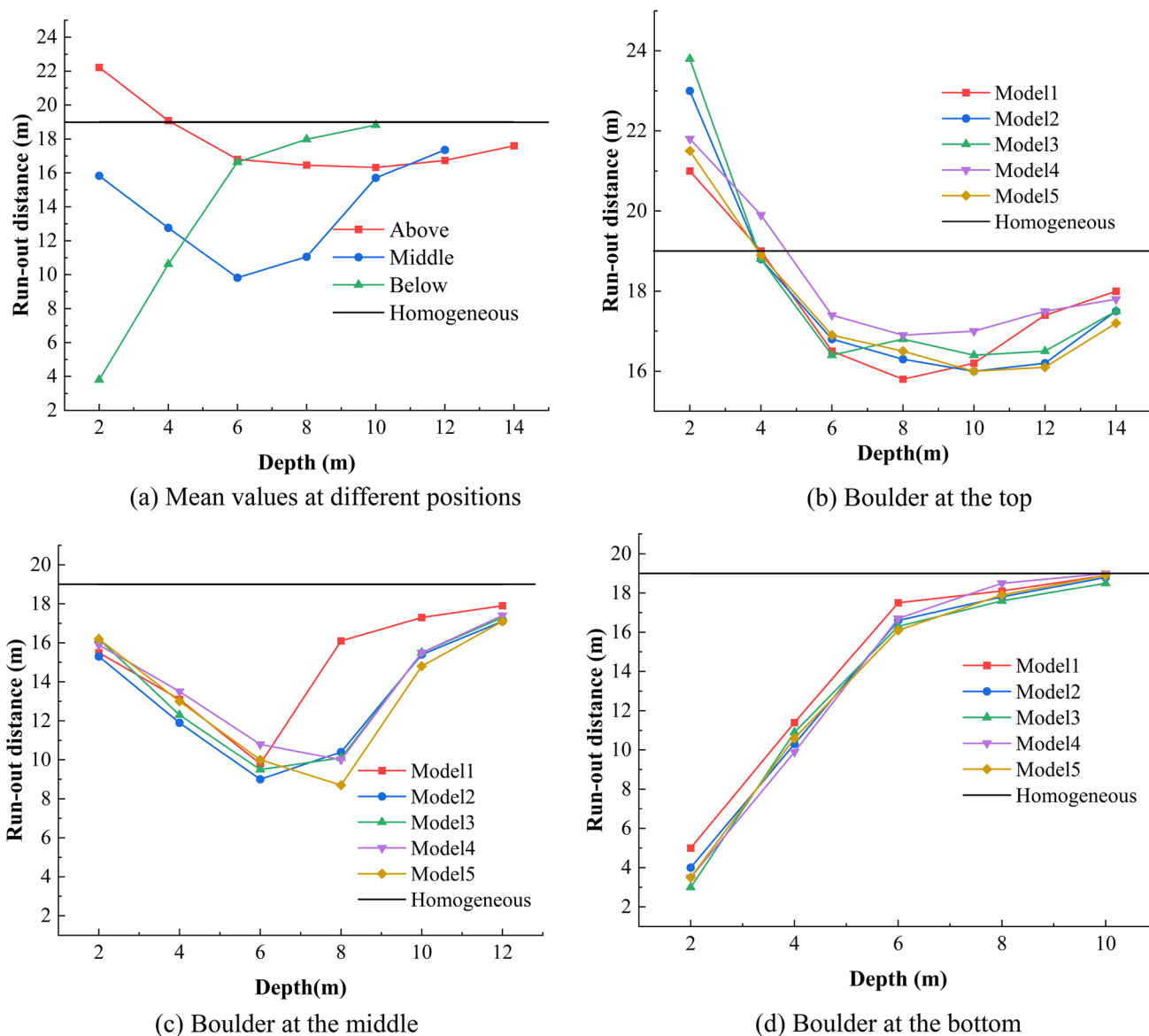(c) Boulder at the middle

(d) Boulder at the bottom

Fig. 14 Run-out distance of the slope when the boulder located at different positions

zero, and only the ith descriptor (where i is equal to 2, 3, or 8) was changed. As shown in Fig. 15, 15 boulder models are generated. To eliminate the influence of the boulder inclination angle, each boulder was rotated 30° for a cycle (12 angles in total), resulting in 180 models. The centre of each boulder was placed at the midpoint of the sliding zone.

Figure 16 displays a boxplot of run-out distance versus Fourier descriptors D_i, with grey points marking the mean values of the run-out distance at different angles connected by a solid line. The following observations were made from the results shown in Fig. 16.

For boulders governed by D_2, the mean value of the run-out distance first slightly increased and then significantly decreased. This is due to the two opposing factors involved in

the boulder influence: the normal interception of the boulder for the soil and the tangential friction between the boulder and two sides of the soil. As shown in Fig. 17, boulders with a smaller D_2 can intercept more widely, but their friction area is smaller, while the boulders with larger D_2 are the opposite effect. Furthermore, the dispersion of the run-out distance caused by the boulder inclination angle increased with an increase in D_2. This is because, when the angle between the long axis of the boulder and the slope surface is close to 90°, the reinforcement effect is stronger, which is significantly different when it is close to 0°. Moreover, elongation increases divergence.

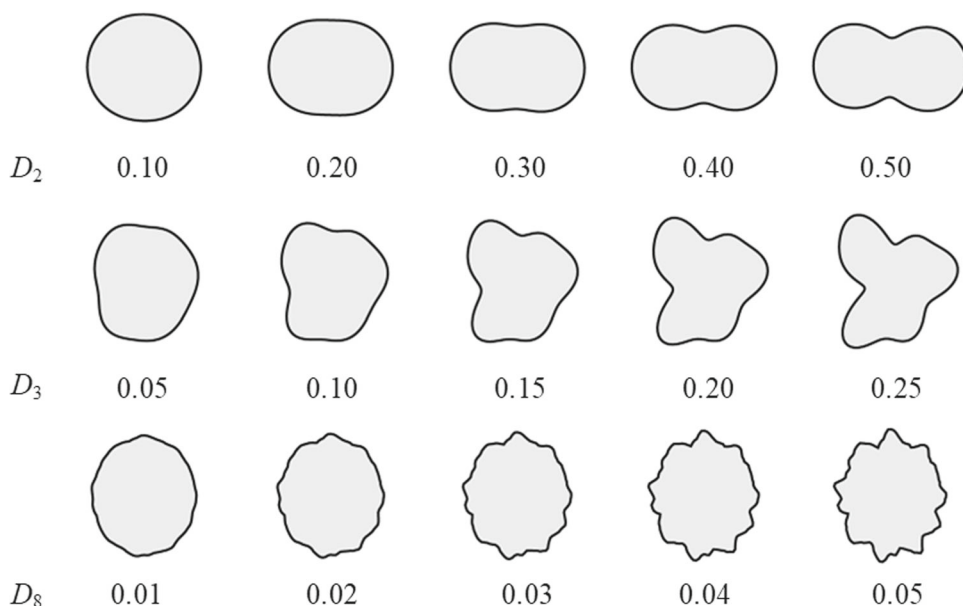**Fig. 15** Fifteen boulder models with different D_i

Fig. 16 Run-out distance under different boulder shapes
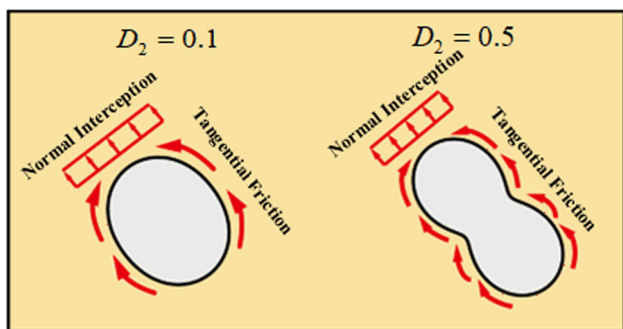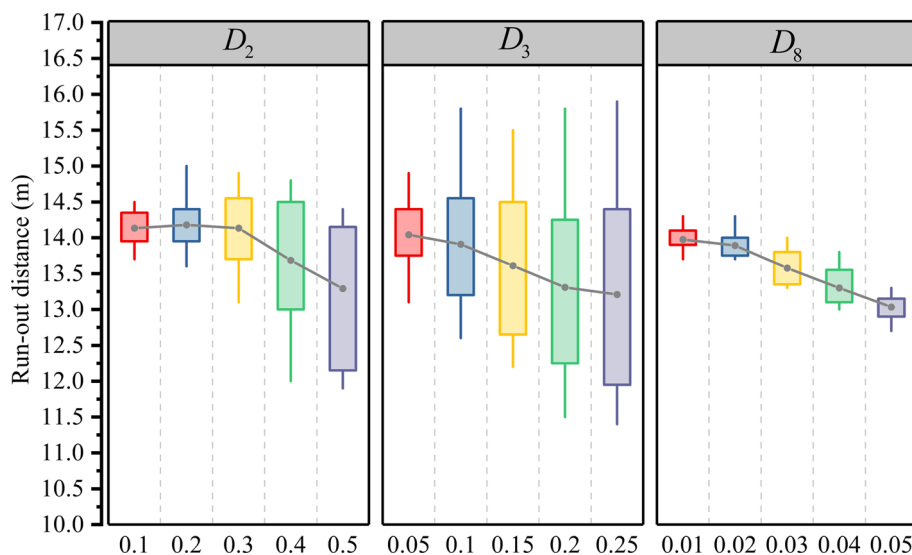

Fig. 17 Schematic of the reinforcement effect of the boulder

For boulders governed by D_3, the run-out distance decreased with increasing D_3. This is because with the increase in D_3, the contact area and occlusion degree between the boulder and soil increase, which improves the reinforcement effect. In addition, owing to the higher uncertainty of the complex shape, the dispersion of the run-out distance increased with an increase in D_3.

For boulders governed by D_8, the run-out distance trend was similar to that of boulders controlled by D_3, and the reasons is also similar. However, unlike convexity, the surface roughness changes more uniformly, causing the dispersion of the run-out distance to change slightly.

(a) Buried depth is 0m   (b) Buried depth is 2m   (c) Buried depth is 6m

(d) Buried depth is 8m   (e) Buried depth is 12m   (f) Homogeneous slope
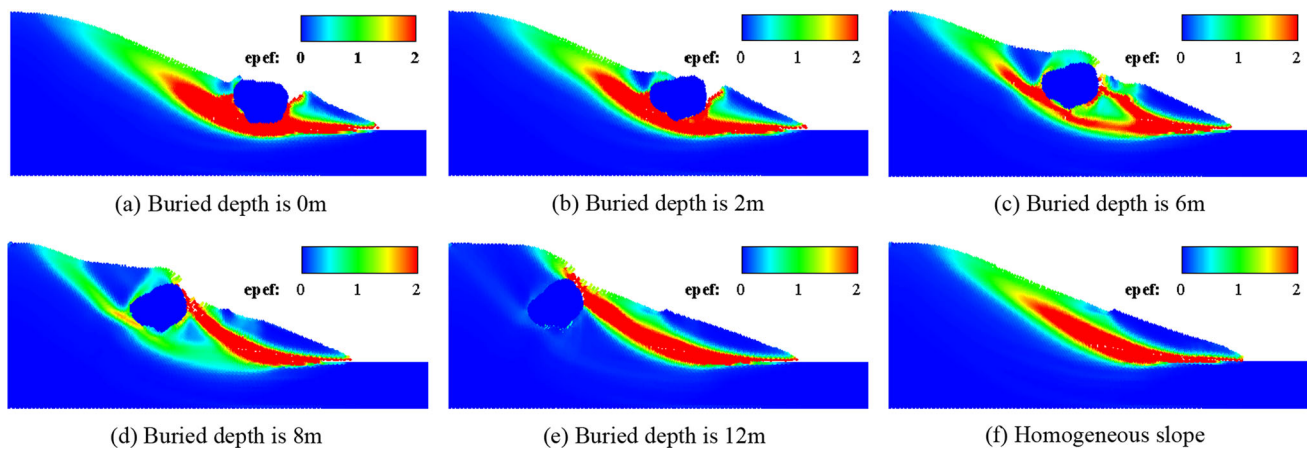
Fig.18 Distribution of the plastic zone of the slope under different buried depths

4.4 Mesoscopic Instability Characteristics of the Slope

In this section, we discuss the influence of the instability characteristics of a solitary boulder slope from two perspectives: final distribution of the plastic zone and its development process.

Figure 18 presents the final distribution of the plastic zone under different boulder-buried depths. When the buried depth is small, the boulder is positioned above the plastic zone, providing almost no reinforcement effect on the slope and even exacerbating instability (seen in Figs. 18a and b). As the buried depth increases, the boulder gradually approaches the sliding zone, causing the plastic zone to wrap around the boulder [39, 40], which enhances the slope stability (seen in Fig. 18c and d). However, when the buried depth continues to increase, the boulder gradually moves under the slope-sliding zone, and its reinforcement effect gradually weakens, resulting in an increase in run-out distance (seen in Fig. 18e).

Figures 19, 20, 21 display the final distribution of the slope plastic zone under boulders with different shapes. The boulder alters the distribution of the slope plastic zone, and an intermediate zone exists where the plastic strain is zero (marked with a red circle in Fig. 19a), with the boulder's reinforcement primarily concentrated in this area. As shown in Fig. 19, as the elongation increases, the intermediate zone narrows, reflecting that the top of the boulder intercepts less soil. From Figs. 20 and 21, the plastic strain fluctuation around the boulder increases with the boulder's convexity and surface roughness, which explains the decrease in the run-out distance with D_3 and D_8 increasing. However, because the fluctuation caused by the surface roughness is uniform, the dispersion of the run-out distance changes only slightly.

Figure 22 illustrates the change in the plastic zone over time during the failure process of the slope. During instability, the plastic zone first appeared near the boulder and

bottom of the slope before expanding along the soil-boulder interface. The plastic zone then further developed to the top of the slope, ultimately leading to transfixation. In practice, it is crucial to reinforce the areas near the bottom of the slope and the boulder.

5 Discussion

In this study, numerous MPM models of solitary boulder slopes were generated using IDFT and boundary recognition. The instability characteristics of the slopes were analysed using a modified MPM program. However, some areas still require further improvement.

Firstly, to simplify the establishment of boulder models and improve the calculation efficiency, all models were assumed to be plane strain models. This simplification of the three-dimensional problem may lead to deviations from the actual situation and therefore needs to be addressed in future research.

Secondly, while this study only considered the impact of solitary boulders on slope stability, there may be smaller stones around the boulder that can also contribute to instability. Further research is needed to investigate the impact of smaller stones on slope stability.

Thirdly, the slope instability in this study only considered the effect of dead weight, whereas other factors, such as earthquakes and rainfall, can also lead to instability. These factors should be the focus of future research.

Fourthly, when the continuous model was discretised into an MPM model, the shape of the model may be distorted, depending on the number of material points used. Increasing the number of material points significantly reduces computational efficiency. Thus, the calculation efficiency of the MPM program must be further improved to enable the calculation of more detailed models.
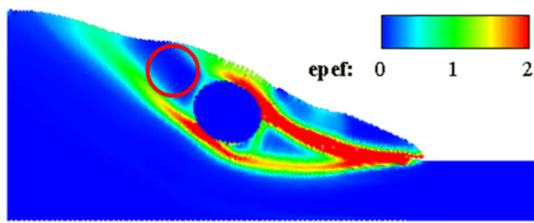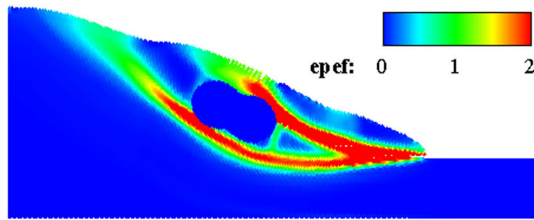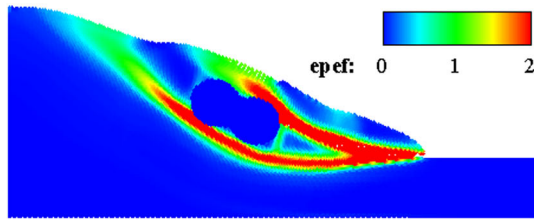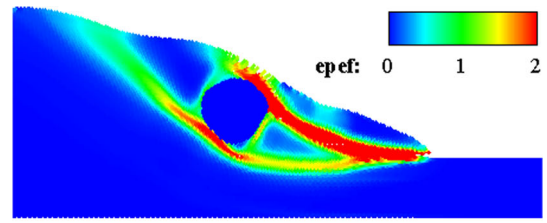
(a) $D_2 = 0.1$
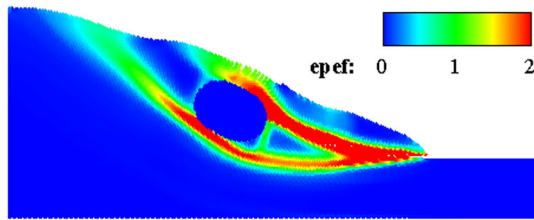
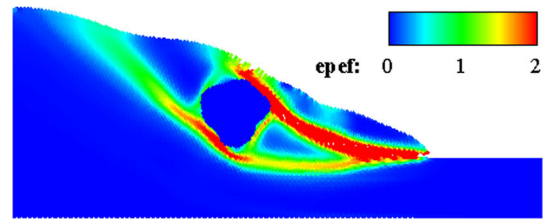(b) $D_2 = 0.2$
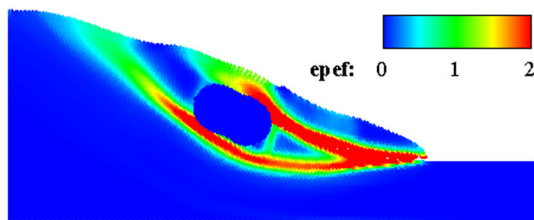
(c) $D_2 = 0.3$

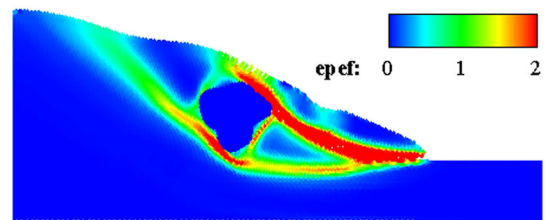(d) $D_2 = 0.4$

(e) $D_2 = 0.5$

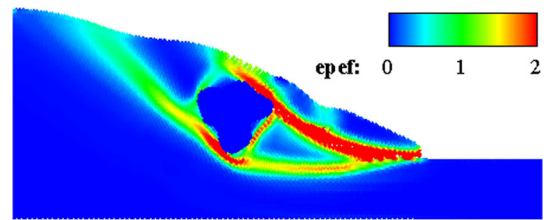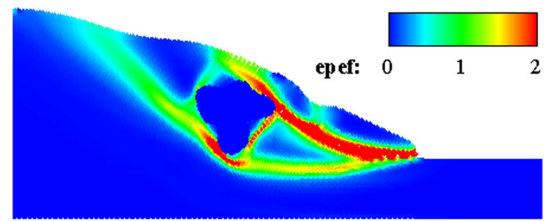**Fig.19** Distribution of the plastic zone of the slope under different D_2

(a) $D_3 = 0.05$

(b) $D_3 = 0.10$

(c) $D_3 = 0.15$

(d) $D_3 = 0.20$

(e) $D_3 = 0.25$

Fig.20 Distribution of the plastic zone of the slope under different D_3

(a) $D_8 = 0.01$

(b) $D_8 = 0.02$

(c) $D_8 = 0.03$
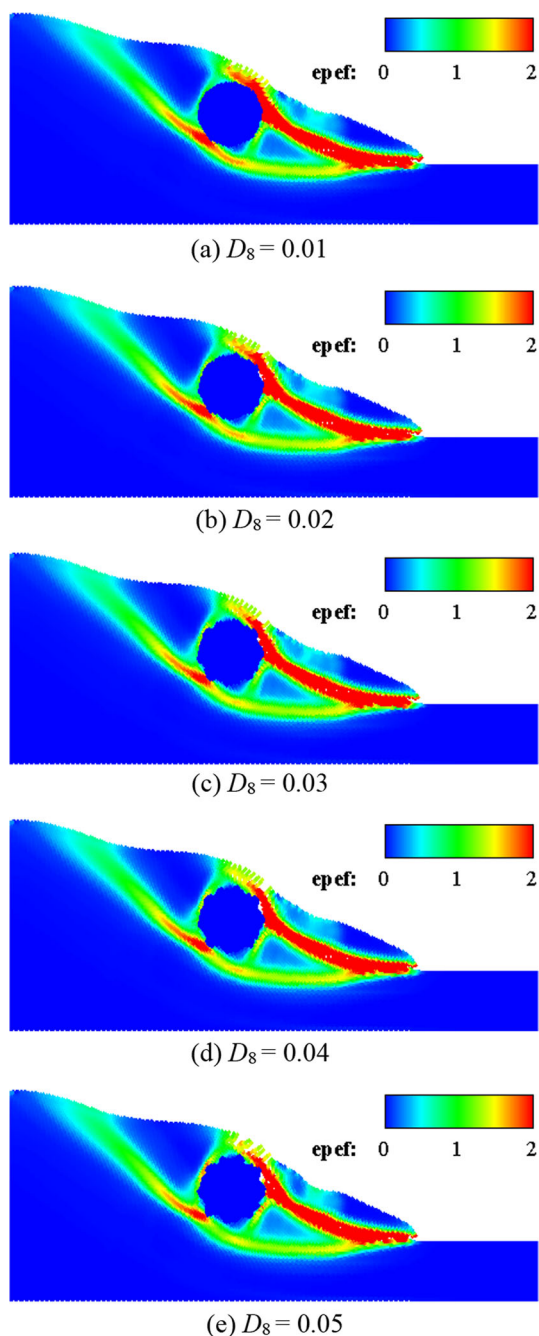
(d) $D_8 = 0.04$

(e) $D_8 = 0.05$

Fig.21 Distribution of the plastic zone of the slope under different D_8

Lastly, the boulder models generated in this paper are of the stellate category, meaning that there is only one intersec-

tion point that radiates from the centroid to the contour of the boulder. This limitation requires further study regarding the generation of more complex boulders.

6 Conclusions

This study aimed to explore the influence of solitary boulders on slope stability by using a modified MPM program. First, laboratory tests were performed to verify the accuracy of the program. Subsequently, boulder models with various shapes were generated using IDFT and incorporated into the slope as MPM models through boundary identification. Finally, the program was used to investigate the large-deformation characteristics of the slope at different boulder positions, shapes, and inclinations. The research findings are summarised as follows:

(1) Boulder at a lower position and closer to the slope-sliding zone enhances the reinforcement effect, resulting in improved slope stability.

(2) The boulder's reinforcement effect is due to its normal interception and tangential friction. Increasing the contact area and degree of occlusion between the boulder and soil can enhance slope stability.

(3) For boulders controlled by elongation and convexity, the dispersion of the run-out distance caused by variations in the boulder inclination angle increases with increasing shape complexity. In contrast, for boulders controlled by surface roughness, where the surface roughness changes uniformly, the dispersion of the run-out distance is not significantly affected.

(4) On a solitary boulder slope, the slope plastic moves around the boulder. However, this effect decays when the distance between the boulder and the sliding zone increases. Even if the boulder is located above the sliding zone, the slope run-out distance may be greater than that of a homogeneous slope.

Although this study has yielded valuable insights, it still exhibits certain limitations. In the future, further refinement of the MPM program will be essential to improve its precision and efficiency. Additionally, improvements are required in the boulder generation procedure to create complex boulders with multiple centres.
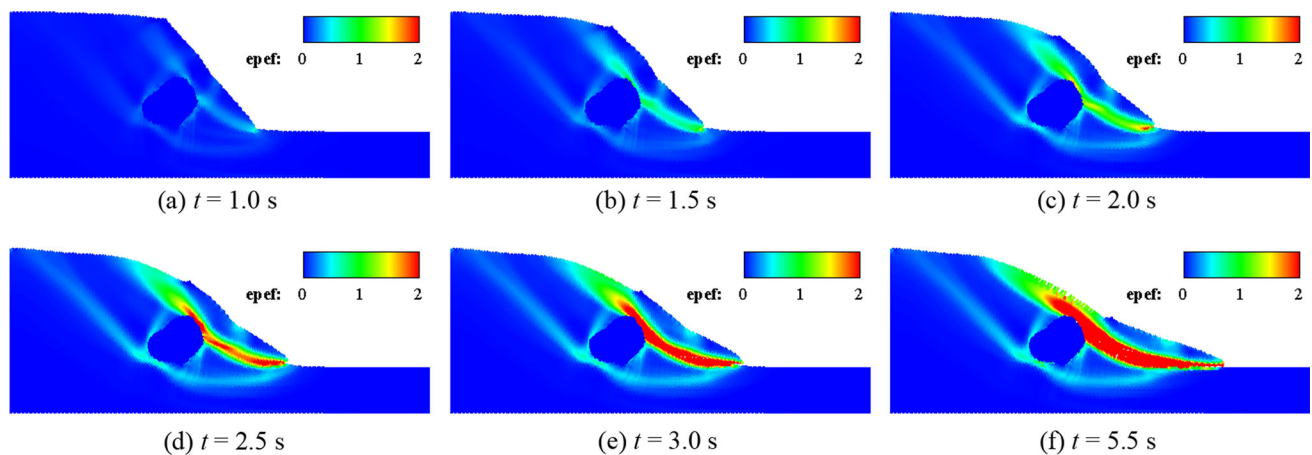
Fig. 22 Development of the plastic zone overtime

Author Contributions LZ contributed to the research methodology and provided guidance for the paper. ZZ carried out the program implementation and data processing, and wrote the initial draft. SW provided some engineering advice for the paper. NQ investigated the research background and provided guidance on the research content. NQ and GL checked and edited the paper.

Data Availability All data included in this study are available upon request by contact with the corresponding.

Declarations

Conflict of interest The authors declare that they have no known competing financial interests or personal relationships that could have appeared to influence the work reported in this paper.

References

1. Koita, M.; Jourde, H.; Koffi, K.; Biaou, A.: Characterization of weathering profile in granites and volcano sedimentary rocks in west Africa under humid tropical climate conditions. Case of the Dimbokro catchment (Ivory coast). J. Earth Syst. Sci. **122**, 841–854 (2013). https://doi.org/10.1007/s12040-013-0290-2
2. Chen, M.; Shen, S.L.; Wu, H.N.; Wang, Z.F.; Suksun, H.: Geotechnical characteristics of weathered granitic gneiss with geo-hazards investigation of pit excavation in Guangzhou, China. Bull. Eng. Geol. Env. **76**, 681–694 (2017). https://doi.org/10.1007/s10064-016-0915-1
3. Hirata, Y.; Chigira, M.; Chen, Y.: Spheroidal weathering of granite porphyry with well-developed columnar joints by oxidation, iron precipitation, and rindlet exfoliation. Earth. Surf. Proc. Land. **42**(4), 657–669 (2017). https://doi.org/10.1002/esp.4008
4. Alejano, L.R.; Pérez-Rey, I.; Múñiz-Menéndez, M., et al.: Considerations relevant to the stability of granite boulders. Rock Mech.
5. Pérez-Rey, I.; Riquelme, A.; González-deSantos, L.M., et al.: A multi-approach rockfall hazard assessment on a weathered granite natural rock slope. Landslides **16**, 2005–2015 (2019). https://doi.org/10.1007/s10346-019-01208-5
6. Pérez-Rey, I.; Alejano, L.R.; Riquelme, A.; González-deSantos, L.: Failure mechanisms and stability analyses of granitic boulders focusing a case study in Galicia (Spain). Int. J. Rock Mech. Min. Sci. **119**, 58–71 (2019). https://doi.org/10.1016/j.ijrmms.2019.04.009
7. Vann, J. D.; Olaiz, A. H.; Morgan, S.; Zapata, C.: A practical approach to a reliability-based stability evaluation of precariously balanced granite boulders. In: 53rd US Rock Mechanics Geomechanics Symposium (2019)
8. Gentilini, C.; Gottardi, G.; Govoni, L.; Mentani, A.; Ubertini, F.: Design of falling rock protection barriers using numerical models. Eng. Struct. **50**, 96–106 (2013). https://doi.org/10.1016/j.engstruct.2012.07.008
9. Morales, T.; Clemente, J.A.; Mollá, L.D.; Izagirre, E.; Jesus, A.U.: Analysis of instabilities in the Basque coast geopark coastal cliffs for its environmentally friendly management (Basque-Cantabrian basin, northern Spain). Eng. Geol. **283**, 106023 (2021). https://doi.org/10.1016/j.enggeo.2021.106023
10. Xu, W.; Yue, Z.; Hu, R.: Study on the mesostructure and mesomechanical characteristics of the soil–rock mixture using digital image processing based finite element method. Int. J. Rock Mech. Min. Sci. **45**(5), 749–762 (2008). https://doi.org/10.1016/j.ijrmms.2007.09.003
11. Gong, J.; Liu, J.: Analysis on the mechanical behaviors of soil–rock mixtures using discrete element method. Procedia Eng. **102**, 1783–1792 (2015). https://doi.org/10.1016/j.proeng.2015.01.315
12. Li, L.; Zhu, J.; Zhao, L.; Hu, S.; Zuo, S.: Numerical analysis on stability and failure characteristics of soil slope containing solitary stone. J. Saf. Sci. Technol. **17**(08), 43–49 (2021). https://doi.org/10.1016/j.enggeo.2013.11.004
13. Liu, X.; Wei, B.; Tang, H.; Dai, Z.: Study on stability and failure mechanism of spheric weathered granite slope. J. Railw Sci. Eng. **16**(12), 2977–2983 (2019). https://doi.org/10.1016/j.ijrmms.2019.04.009
14. Conte, E.; Pugliese, L.; Troncone, A.: Post-failure stage simulation of a landslide using the material point method. Eng. Geol. **253**, 149–159 (2019). https://doi.org/10.1016/j.enggeo.2019.03.006

15. Dan, M.F.M.; Mohamad, E.T.; Komoo, I.: Characteristics of boulders formed in tropical weathered granite: a review. Jurnal Teknologi **78**, 23–30 (2016). https://doi.org/10.11113/jt.v78.9635

16. Dan, M.F.M.; Muhamad, E.T.; Komoo, I., et al.: Physical characteristics of boulders formed in the tropically weathered granite. Jurnal Teknologi **72**(3), 75–82 (2015)

17. Cundall, P.A.; Strack, O.D.L.: Discussion: a discrete numerical model for granular assemblies[J]. Géotechnique. **30**(3), 331–336 (1980). https://doi.org/10.1680/geot.1980.30.3.331

18. Shi, G.: Discontinuous deformation analysis: a new numerical model for the statics and dynamics of deformable block structures. Eng. Comput. **9**, 157–168 (1992). https://doi.org/10.1108/eb023855

19. Gingold, R.A.; Monaghan, J.J.: Smoothed particle hydrodynamics: theory and application to non-spherical stars. Mon. Not. R. Astron. Soc. **181**(3), 375–389 (1977). https://doi.org/10.1093/mnras/181.3.375

20. Sulsky, D.; Chen, Z.; Schreyer, H.L.: A particle method for history-dependent materials. Comput. Methods Appl. Mech. Eng. **118**(1–2), 179–196 (1994). https://doi.org/10.1016/0045-7825(94)90112-0

21. Bardenhagen, S.G.; Kober, E.M.: The generalized interpolation material point method. Comput. Model. Eng. Sci. **5**(6), 477–496 (2004). https://doi.org/10.3970/cmes.2004.005.477

22. Soga, K.; Alonso, E.; Yerro, A.; Kumar, K.; Bandara, S.: Trends in large-deformation analysis of landslide mass movements with particular emphasis on the material point method. Géotechnique. **66**(3), 248–273 (2016). https://doi.org/10.1680/jgeot.15.LM.005

23. Zhao, L.; Qiao, N., et al.: Numerical investigation of the failure mechanisms of soil–rock mixture slopes by material point method. Comput. Geotech. **150**, 104898 (2022). https://doi.org/10.1016/j.compgeo.2022.104898

24. Liu, L.; Zhang, P.; Zhang, S., et al.: Efficient evaluation of run-out distance of slope failure under excavation. Eng. Geol. **306**, 106751 (2022). https://doi.org/10.1016/j.enggeo.2022.106751

25. Coetzee, C.J.; Vermeer, P.A.; Basson, A.H.: The modelling of anchors using the material point method. Int. J. Numer. Anal. Meth. Geomech. **29**(9), 879–895 (2005). https://doi.org/10.1002/nag.439

26. Mollon, G.; Zhao, J.: Fourier-Voronoi-based generation of realistic samples for discrete modelling of granular materials. Granul. Matter **14**(5), 621–638 (2012). https://doi.org/10.1007/s10035-012-0356-x

27. Mollon, G.; Zhao, J.: Generating realistic 3D sand particles using fourier descriptors[J]. Granul. Matter **15**, 95–108 (2013). https://doi.org/10.1007/s10035-012-0380-x

28. Zhao, L.; Huang, D.; Dan, H.; Zhang, S.; Li, D.: Reconstruction of granular railway ballast based on inverse discrete Fourier transform method. Granul. Matter **19**, 1–17 (2017). https://doi.org/10.1007/s10035-017-0761-2

29. Bardenhagen, S.G.: Energy conservation error in the material point method for solid mechanics. J. Comput. Phys. **180**(1), 383–403 (2002). https://doi.org/10.1006/jcph.2002.7103

30. Zhang, X.; Chen, Z.; Liu, Y.: The material point method: a continuum-based particle method for extreme loading cases. Academic Press (2016)

31. Bardenhagen, S.G.; Brackbill, J.U.; Sulsky, D.: The material-point method for granular materials. Comput. Methods Appl. Mech. Eng. **187**(3–4), 529–541 (2000). https://doi.org/10.1016/S0045-7825(99)00338-2

32. Bardenhagen, S.G.; Guilkey, J.E.; Roessig, K.M., et al.: An improved contact algorithm for the material point method and application to stress propagation in granular material. CMES-Comput. Model. Eng. Sci. **2**(4), 509–522 (2001). https://doi.org/10.3970/cmes.2001.002.509

33. Huang, P.; Zhang, X.; Ma, S.; Huang, X.: Contact algorithms for the material point method in impact and penetration simulation. Int. J. Numer. Meth. Eng. **85**(4), 498–517 (2011). https://doi.org/10.1002/nme.2981

34. Ma, Z.; Zhang, X.; Huang, P.: An object-oriented MPM framework for simulation of large-deformation and contact of numerous grains. Comput. Model. Eng. Sci. (CMES) **55**(1), 61 (2010). https://doi.org/10.3970/cmes.2010.055.061

35. Suwal, L.P.; Kuwano, R.: Statically and dynamically measured Poisson's ratio of granular soils on triaxial laboratory specimens. Geotech. Test. J. **36**(4), 493–505 (2013). https://doi.org/10.1520/GTJ20120108

36. Xu, K.; Gu, X.; Hu, C.; Lu, L.: Comparison of small-strain shear modulus and young's modulus of dry sand measured by resonant column and bender–extender element. Can. Geotech. J. **57**(11), 1745–1753 (2020). https://doi.org/10.1139/cgj-2018-0823

37. Liu, X.; Zou, D., et al.: Experimental study to evaluate the effect of particle size on the small strain shear modulus of coarse-grained soils. Measurement **163**, 107954 (2020). https://doi.org/10.1016/j.measurement.2020.107954

38. Liu, X.; Wang, Y.; Li, D.: Investigation of slope failure mode evolution during large-deformation in spatially variable soils by random limit equilibrium and material point methods. Comput. Geotech. **111**, 301–312 (2019). https://doi.org/10.1016/j.compgeo.2019.03.022

39. Liu, S.; Huang, X.; Zhou, A.; Hu, J.; Wang, W.: Soil–rock slope stability analysis by considering the nonuniformity of rocks. Math. Probl. Eng. **2018**, 1–15 (2008). https://doi.org/10.1155/2018/3121604

40. Huang, X.; Yao, Z.; Wang, W.; Zhou, A.; Jiang, P.: Stability analysis of soil-rock slope (SRS) with an improved stochastic method and physical models. Environ. Earth Sci. **80**, 1–21 (2021). https://doi.org/10.1007/s12665-021-09939-2